

Large anomalous Hall effect and A -phase in hexagonal polar magnet $\text{Gd}_3\text{Ni}_8\text{Sn}_4$

Arnab Bhattacharya,^{1,*} Afsar Ahmed,¹ Apurba Dutta,² Ajay Kumar,³ Anis Biswas,^{3,†} Yaroslav Mudryk,³ and I. Das¹

¹*Condensed Matter Physics Division, Saha Institute of Nuclear Physics,*

A CI of Homi Bhabha National Institute, 1/AF, Bidhannagar, Kolkata 700064, India

²*Department of Physics, Indian Institute of Technology, Kanpur 208016, India*

³*Ames National Laboratory, Iowa State University, Ames, Iowa 50011, USA*

While recent theoretical studies have positioned noncollinear polar magnets with C_{nv} symmetry as compelling candidates for realizing topological magnetic phases and substantial intrinsic anomalous Hall conductivity, experimental realizations of the same in strongly correlated systems remain rare. Here, we present a large intrinsic anomalous Hall effect and extended topological magnetic ordering in $\text{Gd}_3\text{Ni}_8\text{Sn}_4$ with hexagonal C_{6v} symmetry. Observation of topological Hall response, corroborated by metamagnetic anomalies in isothermal magnetization, peak/hump features in field-evolution of ac susceptibility and longitudinal resistivity, attests to the stabilization of skyrmion A -phase. The anomalous Hall effect is quantitatively accounted for by the intrinsic Berry curvature-mediated mechanism. Our results underscore polar magnets as a promising platform to investigate a plethora of emergent electrodynamic responses rooted in the interplay between magnetism and topology.

Integrating topology into magnetism has driven a fervent quest for novel quantum materials with exotic electronic and magnetic phases, aimed at unveiling their electrodynamic responses[1–4]. In particular, topological magnets with non-trivial electronic band crossings proximate to Fermi level[5–7], exhibit remarkable properties such as large magnetoresistance, enhanced intrinsic anomalous Hall conductivity (AHC) and anomalous Hall angle[7–14], thus positioning these materials as forerunners to explore the intertwining of topology and strong correlations[15]. In the real-space scenario, quantized topological defects in magnetic spin-lattice, such as skyrmions[16] and antiskyrmions[17], characterized by finite scalar spin chirality $\chi_{ijk} = \mathbf{S}_i \cdot (\mathbf{S}_j \times \mathbf{S}_k)$, where \mathbf{S}_n are the neighbouring spins, induce an additional measurable component to the transverse resistivity (ρ_{xy}), ρ_{xy}^T , referred to as the topological Hall effect (THE)[18–21]. This anomaly occurs as conduction electrons pick up a quantum mechanical Berry phase on coupling with the topological spin structure generated emergent gauge field, B_{eff} , in correlated systems[16]. However, the account of AHC, rooted in non-trivial electronic topology, has primarily centred on centrosymmetric collinear ferromagnets[6, 7], limiting the exploration of coexisting topologically non-trivial incommensurate magnetic ordering and electronic bands. At this juncture, concurrently realizing these magnetic and electronic phenomena is crucial for advancing the understanding of hitherto unexplored interplay, thereby broadening the array of associated topological functionalities[9, 22, 23].

In light of theoretical predictions by Bogdanov *et al.*[24] and Chang *et al.*[25], polar magnets with C_{nv} crystal symmetry have emerged as a compelling platform for realizing this synergy. Contrasting B20 compounds, C_{nv} symmetric materials with quenched orbital moment have a distinct advantage: the asymmetric Dzyaloshinskii-Moriya interaction restricts the magnetic modulation vector perpendicular to the polar axis,

thereby suppressing the formation of competing conical phase[26]. This geometric confinement, combined with moderate easy-plane anisotropy, facilitates stabilising an extended Néel-type skyrmion phase, under an appropriate magnetic field along the polar axis[27–29]. Nevertheless, exploring skyrmion A -phase in bulk polar magnets has predominantly been confined to insulating lacunar spinels [28, 29], limiting the investigation of associated electrodynamic responses[30]. This constraint underscores the need to broaden the material basis to include correlated bulk polar magnets with A -phase.

Here we address this pursuits by achieving extended A -phase down to lowest measured temperature along with substantial intrinsic AHC in $\text{Gd}_3\text{Ni}_8\text{Sn}_4$, a member of $R_3T_8\text{Sn}_4$ family (R and T being rare-earth and $3d$ elements, respectively) of C_{6v} point group, satisfying the prerequisites to host non-trivial magnetic ordering[24], through detailed experimental study. Observed topological Hall response, corroborated by distinct metamagnetic step-like anomalies in isothermal magnetization and peak/hump features in the field evolution of ac susceptibility, is suggestive of the field-induced stabilization of A -phase. Specific heat measurements confirm a long-range spin-modulated ground state. Furthermore, the Berry curvature mediated large intrinsic AHC underscores the $R_3T_8\text{Sn}_4$ family of metallic polar magnets as a unique backdrop for simultaneously realizing electronic and magnetic topological functionalities.

Rietveld refinement of room temperature powder X-ray diffraction pattern of the samples prepared by conventional arc-melting technique confirms the single-phase nature of $\text{Gd}_3\text{Ni}_8\text{Sn}_4$, which crystallizes in hexagonal polar structure (space group $P6_3mc$) (See SF1 and Table.ST1 of supplementary material [31]). The lattice parameters are in good agreement with the previous report[32]. The crystal structure is a distorted derivative of the BaLi_4 structure (space group $P6_3/mmc$), resulting in the splitting of atomic positions and broken

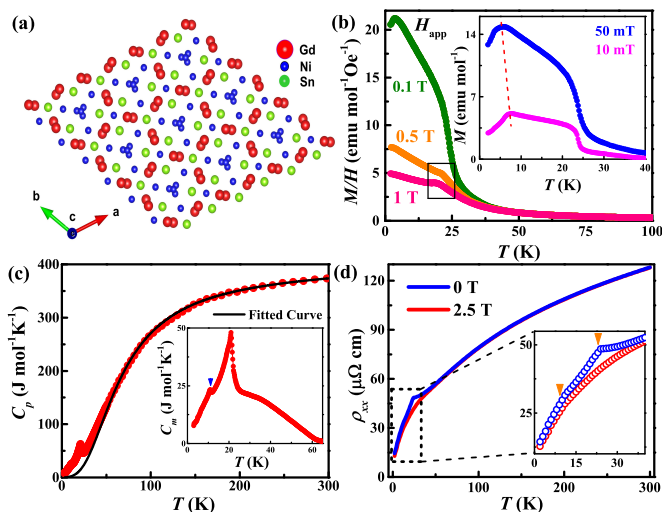


FIG. 1. (a) Crystal structure (top view) of $\text{Gd}_3\text{Ni}_8\text{Sn}_4$. (b) Magnetic susceptibility $\chi(T)$ curves under applied fields of 0.1, 0.5 and 1 T. The magnetization kink is highlighted in black box and the inset shows low-field $M(T)$ curves. (c) Zero-field heat capacity C_p . Black line is the non-magnetic lattice model comprising of electronic contribution and Debye function. Inset shows the $4f$ magnetic contribution to C_p . (d) Temperature variation of ρ_{xx} under H_{app} of 0 and 2.5 T. Inset shows the distinct kinks as mentioned in the text.

inversion (\mathcal{I}) symmetry, with the polar axis along c -axis (Fig.1(a))[33, 34].

To probe the magnetic properties of $\text{Gd}_3\text{Ni}_8\text{Sn}_4$, we performed dc thermomagnetic measurements. Figure.1(b) illustrates the temperature variation of dc magnetic susceptibility ($\chi_{dc} = M/H$) under various applied fields (H_{app}), revealing a transition from paramagnetic to magnetically-ordered state at $T_C = 24$ K under $H_{app} = 10$ mT (inset of Fig.1(b)). $\text{Gd}_3\text{Ni}_8\text{Sn}_4$ follows a Curie-Weiss behaviour with effective paramagnetic moment (μ_{eff}) of $8.11\mu_B/\text{Gd}^{+3}$ ions, slightly larger than theoretical value of $7.94\mu_B$ for free Gd^{+3} ions[35] and a positive Weiss temperature $\Theta_{CW} \approx 18$ K, reflecting the dominant ferromagnetic (FM) correlations. This small difference of μ_{eff} from theoretical value might arise from the involvement of itinerant conduction electrons. A notable decrease in magnetization arises at ($T_K \sim$) 7 K for small H_{app} of 10 mT, persisting up to 0.1 T, with T_K shifting to lower temperatures as H_{app} increases (inset Fig.1(b)). However, the overlapped zero-field cooled (ZFC) and field-cooled (FC) thermomagnetic curves down to 2 K, along with the absence of an upward peak-shift in the real component of ac-susceptibility $\chi'(T)$ across increasing frequencies (Fig.SF2(b) of [31]), collectively rules out the presence of a magnetically frustrated state [32]. This suggests the development of an antiferromagnetic (AFM) component below T_K . However, for this instance, the small H_{app} of 0.15 T is strong enough to melt away

this AFM component. Along with the low-temperature anomaly, adjacent to T_C , a distinct cusp emerges in the intermediate H_{app} of 0.5 and 1 T, followed by an increase in magnetization as temperature decreases (Fig.1(b) and Fig.SF2(a) of [31]). This cusp broadens with increasing H_{app} , indicating a complex magnetic ordering rather than purely FM state.[36, 37].

Figure.1(c) illustrates specific heat C_p as a function of temperature in the range of 2-300 K. The saturated C_p at room temperature $\sim 373.2 \text{ Jmol}^{-1}\text{K}^{-1}$ is in good alignment with the Dulong-Petit limit of $C_p = 3nR = 374.13 \text{ Jmol}^{-1}\text{K}^{-1}$, where R is the ideal gas constant and $n = 15$ is the number of atoms per formula unit. Above 60 K, the C_p can be well-accounted by the band electron component (C_{el}) and phononic Debye model (C_{Deb}) as, $C_{mod} = C_{el} + C_{Deb} = \gamma_{el} \cdot T + 9N_D R (\frac{T}{\theta_D})^3 \int_0^{\theta_D/T} \frac{x^4 e^x}{(e^x - 1)^2} dx$ [38, 39]. Here, γ_{el} , N_D and θ_D are Sommerfeld coefficient, number of Debye oscillator and Debye temperature, respectively. The model fitting of $C_p(T)$, as in Fig.1(c), estimates $\theta_D = 269.3$ K and $\gamma_{el} = 56 \text{ mJmol}^{-1}\text{K}^{-2}$. To discern the $4f$ magnetic contribution (C_m) to C_p , we subtracted the extrapolated model curve to low temperatures, $C_m = C_p - C_{mod}$ (Inset Fig.1(c)). The pronounced λ -peak at $T \sim 21$ K, slightly below T_C , attests to the long-range nature of the magnetic ordering while a subsequent anomaly at lower temperatures corroborates with T_K . Accounting in the mean-field theory concerning the behavior of C_m for localized moment systems[40, 41], equal moment arrangement of Gd^{+3} ions with $J = 7/2$ should yield $C_m^{\text{MFT}} = \frac{5S(S+1)}{2J^2+2J+1}R = 20 \text{ Jmol}^{-1}\text{K}^{-1}$. Contrary to this prediction, the observed C_m peak ($\sim 16 \text{ Jmol}^{-1}\text{K}^{-1}/\text{Gd}^{+3}$) is much smaller than C_m^{MFT} , indicating a more complex modulated magnetic ordering than conventional equal-moment magnetic ground state[42–46], endorsing the magnetization results.

Figure.1(d) depicts the temperature dependence of longitudinal resistivity (ρ_{xx}) under 0 and 2.5 T H_{app} with a residual resistivity ratio ($=\rho_{300\text{K}}/\rho_{2\text{K}}$) of 8.8 indicating the high quality of prepared samples. Notably, $\rho_{xx}(T)$ under 0 T exhibits a distinct peak at T_C , marking the onset of long-range ordering, followed by a rapid decrease due to the suppression of spin-disorder scattering. Above T_C , $\rho_{xx}(T)$ shows an upturn, attributable to enhanced spin-fluctuations due to short-range Gd- $4f$ correlations prior to long-range ordering[3, 44–47], while it also captures the second transition at T_K . However, the peak at T_C melts away with the application of 2.5 T, establishing an intricate correlation between magnetic ordering and transport properties.

To elucidate the field-induced modifications in magnetic ordering, we investigate the isothermal dc-magnetization $M(H)$ (in Fig.2(a)). The magnetization profile reveals distinct metamagnetic step-like anomalies before attaining the field-polarized state. Notably, these

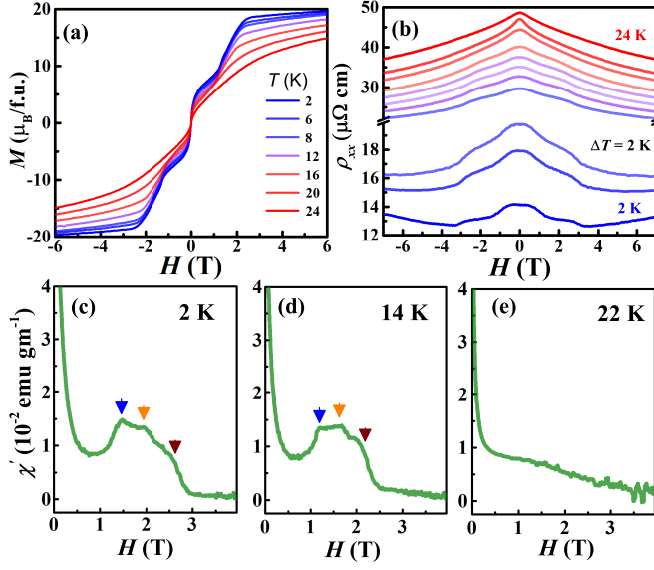


FIG. 2. (a) Isothermal magnetization M as a function of applied magnetic field. (b) Isothermal $\rho_{xx}(H)$ showcasing anomaly associated with phase transition below T_C . (c)-(e) Field dependant ac-susceptibility measured at different temperatures.

metamagnetic features weaken as T increases and approaches T_C but persist on either side of T_K , implying a robust field-induced stabilization of complex magnetic ordering[3, 48, 49]. Intriguingly, isothermal $\rho_{xx}(H)$ as illustrated in Fig.2(b), displays a pronounced change of slope at fields corresponding to the metamagnetic transitions, driven by significant alterations of carrier lifetime due to domain wall scattering associated with these magnetic transitions[3, 48, 49]. To gain further insight into these metamagnetic transitions we analyzed the field-evolution of ac-susceptibility, $\chi'(H)$, which has been extensively employed to characterize various topologically trivial and non-trivial magnetic phases due to associated changes in the energy landscape[50–53]. Figure.2(c)-(e) illustrates the $\chi'(H)$ under an applied ac frequency of 333 Hz at different temperatures. Pronounced peak/dip anomalies (marked by arrows) are evident at fields corresponding to the metamagnetic transitions in isothermal dc-magnetization and $\rho_{xx}(H)$ at 2 K and 14 K but vanish completely at 22 K. Following these anomalies, $\chi'(H)$ exhibit monotonous behavior as $\text{Gd}_3\text{Ni}_8\text{Sn}_4$ attains a field-polarized state. It is noteworthy, similar features in $\chi'(H)$ have been reported for Gd_2PdSi_3 [54] and D_{2d} Heusler alloys[55, 56], across their skyrmion and anti-skyrmion phase pocket, respectively. The persistence of these peak/dip anomalies across different temperatures in $\chi'(H)$ underscores the field-driven stabilization of a robust extended topological A -phase which subsequently melts to a field-polarized state under high H_{app} .

Building on the established correlation between topo-

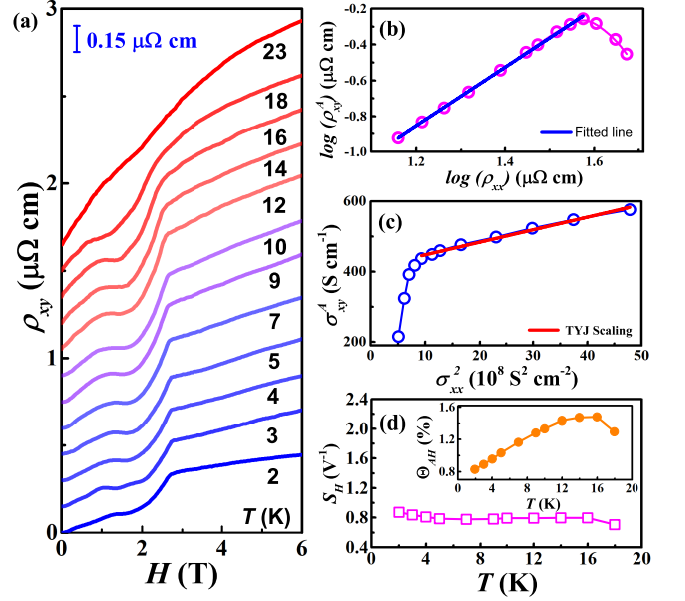


FIG. 3. (a) Field dependant isothermal ρ_{xy} at various T . For better visualization, an offset has been created along ρ_{xy} axis. (b) $\log(\rho_{xy}^A)$ versus $\log(\rho_{xx})$ with the slope of $\alpha \approx 1.63$ (c) TYJ scaling plot for AHC. (d) T variation of the anomalous Hall coefficient S_H . Inset depicts the T dependency of anomalous Hall angle Θ_{AH}

logical A -phase and $\rho_{xy}(H)$ [16, 18, 19], we turn to the Hall transport data. Figure.3(a) illustrates the field dependence of ρ_{xy} at various T . For magnetic conductors with non-trivial magnetic orderings, ρ_{xy} is empirically expressed as, $\rho_{xy} = \rho_{xy}^N + \rho_{xy}^A + \rho_{xy}^T$, where $\rho_{xy}^N = R_0 H$ and $\rho_{xy}^A = R_s M$ are normal and anomalous Hall resistivity with coefficients R_0 and R_s , respectively. The positive slope of $\rho_{xy}(H)$ attests to holes as majority charge carriers with a carrier density of $n_0 \sim 2 \times 10^{22} \text{ cm}^{-3}$ at $T = 2 \text{ K}$, inferred from the relation $n_0 = -1/|e|R_0$. ρ_{xy}^A is obtained by high field extrapolation of $\rho_{xy}(H)$, where magnetization attains saturation, to zero field (Fig. SF3(a) of [31]). Figure.SF3(b) of [31] illustrates a monotonic temperature variation of ρ_{xy}^A . In a general framework, AHE can stem from reciprocal space originated Berry curvature driven intrinsic or asymmetric scattering induced extrinsic side-jump (sj)/skew-scattering (sk) mechanisms or a combination of both, where depending upon origin, ρ_{xy}^A scales differently with ρ_{xx} [57]. In Fig.3(b), the $\log(\rho_{xy}^A)$ vs. $\log(\rho_{xx})$ curve is fitted using the linear relation $\rho_{xy} \propto \rho_{xx}^\alpha$ which yields $\alpha \approx 1.63$, validating the dominant contribution from intrinsic or sj mechanism in AHE[58]. For a better insight into the dominating contribution, we derive the AHC, σ_{xy}^A , from total Hall conductivity $\sigma_{xy} \approx \rho_{xy}/\rho_{xx}^2$, employing method analogous to obtaining ρ_{xy}^A . The near temperature-invariant nature exhibited by σ_{xy}^A (Fig.SF3(b) of [31]), with a value

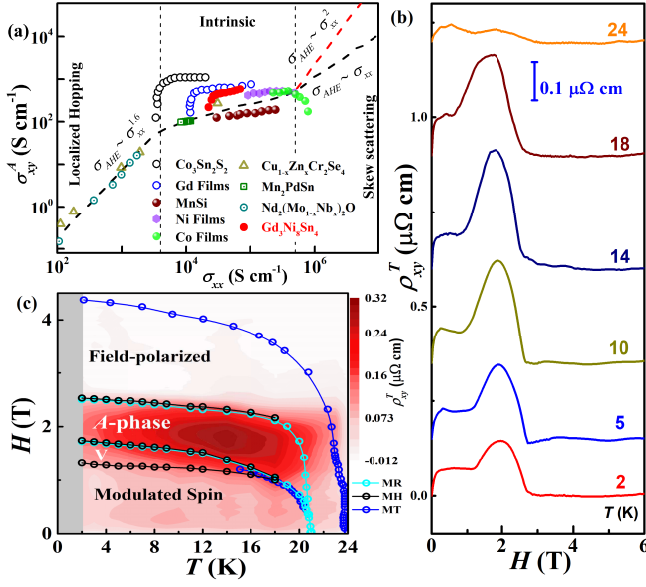


FIG. 4. (a) Universal plot of σ_{xy}^A with σ_{xx} , illustrating the intrinsic regime for $\text{Gd}_3\text{Ni}_8\text{Sn}_4$ along with other magnetic conductors (b) Field dependency of ρ_{xy}^T , suggesting the formation of topological magnetic ordering. A vertical offset has been created for clear presentations. (c) Contour plot of ρ_{xy}^T in H - T diagram with the phase boundaries obtained from the derivative of $\chi_{dc}(T)$, isothermal $M(H)$ and $\rho_{xx}(H)$.

of $\sim 577 \text{ S cm}^{-1}$ at $T = 2 \text{ K}$, is suggestive of the intrinsic origin of AHE[12–14]. To quantify the different contributions, we adopt the Tian-Ye-Jin scaling relation for σ_{xy}^A *i.e.*, $\sigma_{xy}^A = -\kappa\sigma_{xx0}^{-1}\sigma_{xx}^2 - b = -a\sigma_{xx}^2 - b$ [58]. Here, σ_{xx0} and $b = \rho_{xy}^A/\rho_{xx}^2$ corresponds to residual longitudinal conductivity and intrinsic AHC $\sigma_{xy, \text{int}}^A$, respectively. The scaling expects a linear relation of σ_{xy}^A with σ_{xx}^2 , illustrated in Fig.3(c), with the intercept yielding $b \approx 413 \text{ S cm}^{-1}$. The deviation from scaling as T approaches T_C can originate from the broadening of the Fermi-Dirac distribution[6, 9]. Thus, $\sigma_{xy, \text{int}}^A$ accounts to 71% of σ_{xy}^A at $T = 2 \text{ K}$, underpinning the dominance of Berry curvature-driven contribution. However, at low temperatures *sj* conductivity, $\sigma_{xy, \text{sj}}^A$, remains closely intertwined with $\sigma_{xy, \text{int}}^A$ due to reduced phonon scattering, complicating individual quantification in the absence of theoretical framework. While the estimation of the order of magnitude of $\sigma_{xy, \text{sj}}^A$ shows that it is two orders smaller than $\sigma_{xy, \text{int}}^A$ [57, 59], confirming the dominance of intrinsic mechanism in AHE.

Figure.3(d) illustrates temperature variation of the anomalous Hall coefficient $S_H (= \sigma_{xy}^A/M)$, quantifying the sensitivity of anomalous Hall current to magnetization. Notably, S_H remains invariant with temperature for $\sim 0.8 \text{ V}^{-1}$, confirming the robustness and insensitivity of AHE to impurity scattering[12]. On employing the second characteristics parameter, *i.e.*, the anomalous Hall

angle, $\Theta_{AH} = \sigma_{xy}/\sigma_{xx}(\%)$, a monotonic increase with temperature is observed (inset of Fig.3(d)). Figure.4(a) shows the variation of σ_{xy}^A with σ_{xx} of $\text{Gd}_3\text{Ni}_8\text{Sn}_4$ along with other magnetic conductors. Here it is well within the intrinsic limit and remains invariant with σ_{xx} , anchoring the Berry curvature rooted picture of AHE[60, 61].

Leveraging the intrinsic origin of AHE, R_S is formulated as $R_S = \gamma\rho_{xx}^2$. Hence, to obtain R_S , we modeled the transverse resistivity as $(\rho_{xy}/H) = R_0 + \gamma(\rho_{xx}^2 M)/H$. The (ρ_{xy}/H) versus $(\rho_{xx}^2 M)/H$ plot showcases a good linear relation in the field-polarized state (Fig.SF3(c) of [31]), with the slope and intercept yielding γ and R_0 , respectively. Figure.4(b) shows the field dependency of ρ_{xy}^T at various T , obtained by subtracting the calculated $(\rho_{xy}^N + \rho_{xy}^A)$ from ρ_{xy} (Fig.SF3(a),(d) of [31]). ρ_{xy}^T attains a maximum value of $0.32 \mu\Omega\text{cm}$ at 14 K ($\sigma_{xy}^T \sim 253 \text{ S cm}^{-1}$) and gradually diminishes with increasing temperature. The evolution of ρ_{xy}^T , as T approaches T_C , attests to the consistency with the scalar spin-chirality model, suggesting a significant contribution of the molecular field from $4f$ -moment on conduction electrons through f - d coupling[62]. Figure.4(c) shows that the peak positions in the derivative of isothermal magnetization $M(H)$, longitudinal resistivity $\rho_{xx}(H)$ and temperature-dependant magnetization $M(T)$ distinctly mark the boundaries of Field-polarized, *A*-phase and modulated spin phase along with a metastable *V*-phase (see Fig.SF4 of [31]). Accounting in the theoretical model proposed by Rowland *et al.*[63] and broken- \mathcal{I} along z -axis, we speculate, a dominant Rashba spin-orbit coupling stabilizes a sliver square skyrmion lattice (*V*-phase) adjacent to dominant *A*-phase. Overlaying ρ_{xy}^T contour plot with the H - T phase diagram shows that the enhanced ρ_{xy}^T exclusively appears in the *A*-phase and *V*-phase region, suggesting H -driven evolution of the spin-modulated ground state to topological spin textures. It is worth mentioning, a shoulder-like anomaly in ρ_{xy}^T adjacent to the peak in the *A*-phase is attributable to the complex modulated ground state magnetic ordering [64].

For a comprehensive perspective, the maximum value of ρ_{xy}^T ($\sim 0.32 \mu\Omega\text{cm}$) is comparable with large wavelength spin-modulated systems like cubic FeGe ($0.16 \mu\Omega\text{cm}$)[65], polar chiral magnet GdPt_2B ($0.14 \mu\Omega\text{cm}$)[36] and D_{2d} Heusler alloy $\text{Mn}_{1.4}\text{Pt}_{0.9}\text{Pd}_{0.1}\text{Ga}$ ($0.4 \mu\Omega\text{cm}$)[55]. This contrasts sharply with Gd-based centrosymmetric compounds like Gd_2PdSi_3 [3], $\text{Gd}_3\text{Ru}_4\text{Al}_{12}$ [48] and GdRu_2Si_2 [49] with short-period spin modulation wavelength squeezing the skyrmions to smaller sizes. Accounting in the theory of THE[66], the real space Berry curvature primarily contributes to the limit $l < a_t$, where $l = \frac{\hbar}{n_0 e^2} (3\pi^2 n_0)^{\frac{1}{3}} \sigma_{xx0}$ and a_t are the mean-free path of electrons and size of skyrmion, respectively. To verify this, we performed a semiquantitative analysis of THE, drawing on the established topological nature of the *A*-phase. In continuum approximation for smooth winding

spin texture, the B_{eff} is defined as $B_{eff} = h/ea_t$ and is related to ρ_{xy}^T by spin polarization P of conduction electron and normal Hall coefficient R_0 , $\rho_{xy}^T = B_{eff}PR_0$ [16]. The conduction electron polarization can be crudely estimated as $P = M_{spo}/M_S$, where M_{spo} is the ordered moment in the A -phase, by which we arrive at $P = 0.8$. Employing the maximum observed ρ_{xy}^T at 14 K, we derive $B_{eff} \sim 3.7$ T corresponding to $a_t \sim 34$ nm $> l \approx 10$ -15 nm at $\rho_{xx} \sim 35 \mu\Omega cm$, acknowledging the real-space A -phase driven picture of THE while being consistent with the consensus of stabilizing large-sized skyrmion (20-200 nm) by DM interaction[4, 67].

In conclusion, this comprehensive experimental study establishes metallic polar magnets as a conducive backdrop for realizing the topological A -phase and exploring the reciprocal-space mediated emergent electrodynamic responses. The topological Hall effect, supplemented by peak/dip behaviour in field-dependent ac-susceptibility, is attributed to the stabilization of an extended topological magnetic quasiparticle phase of Néel-type skyrmion, as per theoretical predictions for systems exhibiting C_{nv} symmetry, and a potential narrow square skyrmion phase. These results validate the theoretically-laid phase diagram of skyrmion-hosting polar magnets[63]. Additionally, the quadratic relation between ρ_{xy}^A and ρ_{xx} quantitatively attests to the role of reciprocal-space Berry curvature in generating the substantial AHC, resonating with the possibility of Weyl nodes in moderately \mathcal{T} -broken systems[25, 68]. These findings underscore the broken- \mathcal{T} inherent to the $R_3T_8Sn_4$ family as a compelling framework to explore the non-trivial bulk electronic band topology and non-collinear magnetic ordering. Our findings advocate further experimental and theoretical investigation focused on correlated polar magnets to unravel the intricate interplay of reciprocal-space-mediated electromagnetic fields and magnetization dynamics to leverage topological functionalities.

Acknowledgement A. Bhattacharya and A. Ahmed acknowledge SINP, India and the Department of Atomic Energy (DAE), Government of India for their Fellowship. Work at the Ames National Laboratory was supported by the Division of Materials Science and Engineering of the Office of Basic Energy Sciences, Office of Science of the U.S. Department of Energy (D.O.E). Ames National Laboratory is operated for the U.S. DOE by Iowa State University of Science and Technology under Contract No. DE-AC02-07CH11358. We thank Prof. E. V. Sampathkumaran, TIFR, for his valuable suggestions.

* arnab.bh@saha.ac.in

† anis@ameslab.gov

[1] N. Nagaosa and Y. Tokura, Topological properties and

dynamics of magnetic skyrmions, Nature nanotechnology **8**, 899 (2013).

- [2] K. Manna, Y. Sun, L. Muechler, J. Kübler, and C. Felser, Heusler, Weyl and Berry, Nature Reviews Materials **3**, 244 (2018).
- [3] S. R. Saha, H. Sugawara, T. D. Matsuda, H. Sato, R. Mallik, and E. V. Sampathkumaran, Magnetic anisotropy, first-order-like metamagnetic transitions, and large negative magnetoresistance in single-crystal Gd₂PdSi₃, Phys. Rev. B **60**, 12162 (1999).
- [4] Y. Tokura and N. Kanazawa, Magnetic skyrmion materials, Chemical Reviews **121**, 2857 (2020).
- [5] D. Liu, A. Liang, E. Liu, Q. Xu, Y. Li, C. Chen, D. Pei, W. Shi, S. Mo, P. Dudin, *et al.*, Magnetic Weyl semimetal phase in a kagomé crystal, Science **365**, 1282 (2019).
- [6] I. Belopolski, K. Manna, D. S. Sanchez, G. Chang, B. Ernst, J. Yin, S. S. Zhang, T. Cochran, N. Shumiya, H. Zheng, *et al.*, Discovery of topological Weyl fermion lines and drumhead surface states in a room temperature magnet, Science **365**, 1278 (2019).
- [7] Q. Wang, Y. Xu, R. Lou, Z. Liu, M. Li, Y. Huang, D. Shen, H. Weng, S. Wang, and H. Lei, Large intrinsic anomalous Hall effect in half-metallic ferromagnet Co₃Sn₂S₂ with magnetic Weyl fermions, Nature communications **9**, 1 (2018).
- [8] J. F. Steiner, A. V. Andreev, and D. A. Pesin, Anomalous Hall Effect in Type-i Weyl Metals, Phys. Rev. Lett. **119**, 036601 (2017).
- [9] A. Bhattacharya, M. R. Habib, A. Ahmed, B. Sapat, S. DuttaGupta, I. Dasgupta, and I. Das, Spin-valve-like magnetoresistance and anomalous Hall effect in magnetic Weyl metal Mn₂PdSn, Phys. Rev. B **110**, 014417 (2024).
- [10] C.-Z. Chang, J. Zhang, X. Feng, J. Shen, Z. Zhang, M. Guo, K. Li, Y. Ou, P. Wei, L.-L. Wang, *et al.*, Experimental observation of the quantum anomalous Hall effect in a magnetic topological insulator, Science **340**, 167 (2013).
- [11] K. Kuroda, T. Tomita, M.-T. Suzuki, C. Bareille, A. Nugroho, P. Goswami, M. Ochi, M. Ikhlas, M. Nakayama, S. Akebi, *et al.*, Evidence for magnetic Weyl fermions in a correlated metal, Nature materials **16**, 1090 (2017).
- [12] K. Kim, J. Seo, E. Lee, K.-T. Ko, B. Kim, B. G. Jang, J. M. Ok, J. Lee, Y. J. Jo, W. Kang, *et al.*, Large anomalous Hall current induced by topological nodal lines in a ferromagnetic van der Waals semimetal, Nature materials **17**, 794 (2018).
- [13] P. Li, J. Koo, W. Ning, J. Li, L. Miao, L. Min, Y. Zhu, Y. Wang, N. Alem, C.-X. Liu, *et al.*, Giant room temperature anomalous Hall effect and tunable topology in a ferromagnetic topological semimetal Co₂MnAl, Nature communications **11**, 3476 (2020).
- [14] B. P. Belbase, L. Ye, B. Karki, J. I. Facio, J.-S. You, J. G. Checkelsky, J. Van Den Brink, and M. P. Ghimire, Large anomalous Hall effect in single crystals of the kagome weyl ferromagnet Fe₃Sn, Physical Review B **108**, 075164 (2023).
- [15] S. Paschen and Q. Si, Quantum phases driven by strong correlations, Nature Reviews Physics **3**, 9 (2021).
- [16] A. Neubauer, C. Pfleiderer, B. Binz, A. Rosch, R. Ritz, P. G. Niklowitz, and P. Böni, Topological Hall Effect in the A Phase of MnSi, Phys. Rev. Lett. **102**, 186602 (2009).
- [17] A. K. Nayak, V. Kumar, T. Ma, P. Werner, E. Pippel,

- R. Sahoo, F. Damay, U. K. Röbber, C. Felser, and S. S. Parkin, Magnetic antiskyrmions above room temperature in tetragonal Heusler materials, *Nature* **548**, 561 (2017).
- [18] Q. Du, Z. Hu, M.-G. Han, F. Camino, Y. Zhu, and C. Petrovic, Topological Hall Effect anisotropy in kagome bilayer metal Fe_3Sn_2 , *Phys. Rev. Lett.* **129**, 236601 (2022).
- [19] P. Puphal, V. Pomjakushin, N. Kanazawa, V. Ukleev, D. J. Gawryluk, J. Ma, M. Naamneh, N. C. Plumb, L. Keller, R. Cubitt, E. Pomjakushina, and J. S. White, Topological Magnetic Phase in the Candidate Weyl Semimetal CeAlGe , *Phys. Rev. Lett.* **124**, 017202 (2020).
- [20] Q. Wang, K. J. Neubauer, C. Duan, Q. Yin, S. Fujitsu, H. Hosono, F. Ye, R. Zhang, S. Chi, K. Krycka, H. Lei, and P. Dai, Field-induced topological Hall effect and double-fan spin structure with a c -axis component in the metallic kagome antiferromagnetic compound Ymn_6Sn_6 , *Phys. Rev. B* **103**, 014416 (2021).
- [21] A. Fert, N. Reyren, and V. Cros, Magnetic skyrmions: advances in physics and potential applications, *Nature Reviews Materials* **2**, 1 (2017).
- [22] S.-H. Yang, R. Naaman, Y. Paltiel, and S. S. Parkin, Chiral spintronics, *Nature Reviews Physics* **3**, 328 (2021).
- [23] D. Kurebayashi and K. Nomura, Voltage-driven magnetization switching and spin pumping in Weyl Semimetals, *Phys. Rev. Appl.* **6**, 044013 (2016).
- [24] A. Bogdanov and A. Hubert, Thermodynamically stable magnetic vortex states in magnetic crystals, *Journal of magnetism and magnetic materials* **138**, 255 (1994).
- [25] G. Chang, B. Singh, S.-Y. Xu, G. Bian, S.-M. Huang, C.-H. Hsu, I. Belopolski, N. Alidoust, D. S. Sanchez, H. Zheng, H. Lu, X. Zhang, Y. Bian, T.-R. Chang, H.-T. Jeng, A. Bansil, H. Hsu, S. Jia, T. Neupert, H. Lin, and M. Z. Hasan, Magnetic and noncentrosymmetric Weyl fermion semimetals in the RAlGe family of compounds (R = rare earth), *Phys. Rev. B* **97**, 041104 (2018).
- [26] S. Bordács, A. Butykai, B. G. Szigeti, J. S. White, R. Cubitt, A. O. Leonov, S. Widmann, D. Ehlers, H.-A. K. von Nidda, V. Tsurkan, *et al.*, Equilibrium skyrmion lattice ground state in a polar easy-plane magnet, *Scientific reports* **7**, 7584 (2017).
- [27] D. Singh, Y. Fujishiro, S. Hayami, S. H. Moody, T. Nomoto, P. R. Baral, V. Ukleev, R. Cubitt, N.-J. Steinke, D. J. Gawryluk, *et al.*, Transition between distinct hybrid skyrmion textures through their hexagonal-to-square crystal transformation in a polar magnet, *Nature Communications* **14**, 8050 (2023).
- [28] T. Kurumaji, T. Nakajima, V. Ukleev, A. Feoktystov, T.-h. Arima, K. Kakurai, and Y. Tokura, Néel-type Skyrmion Lattice in the Tetragonal Polar Magnet VOSe_2O_5 , *Phys. Rev. Lett.* **119**, 237201 (2017).
- [29] I. Kézsmárki, S. Bordács, P. Milde, E. Neuber, L. M. Eng, J. S. White, H. M. Rønnow, C. D. Dewhurst, M. Mochizuki, K. Yanai, *et al.*, Néel-type skyrmion lattice with confined orientation in the polar magnetic semiconductor GaV_4S_8 , *Nature materials* **14**, 1116 (2015).
- [30] Z. Li, H. Zhang, G. Li, J. Guo, Q. Wang, Y. Deng, Y. Hu, X. Hu, C. Liu, M. Qin, *et al.*, Room-temperature sub-100 nm néel-type skyrmions in non-stoichiometric van der waals ferromagnet $\text{Fe}_{3-x}\text{GaTe}_2$ with ultrafast laser writability, *Nature Communications* **15**, 1017 (2024).
- [31] See supplementary material: This material includes further auxiliary data on structural refinement, transverse resistivity, ac susceptibility and dc magnetization measurements., Supplementary URL to be added by journal (2024).
- [32] V. Romaka, L. Romaka, I. Romaniv, E. Hlil, Z. Rykavets, and B. Kuzhel, Crystallographic, magnetic and electrical characteristics of $\text{R}_3\text{Ni}_8\text{Sn}_4$ compounds ($R = \text{Y, Nd, Sm, Gd, and Tb}$), *Journal of Alloys and Compounds* **701**, 358 (2017).
- [33] R. Skolozdra, B. Garcia-Landa, D. Fruchart, D. Gignoux, J. Soubeyroux, and L. Akselrud, Very weak itinerant ferromagnetism in the new $\text{Lu}_3\text{Co}_{8-x}\text{Sn}_4$ compound ($x=0.23$), *Journal of alloys and compounds* **235**, 210 (1996).
- [34] R. Takagi, J. White, S. Hayami, R. Arita, D. Honecker, H. Rønnow, Y. Tokura, and S. Seki, Multiple-q non-collinear magnetism in an itinerant hexagonal magnet, *Science advances* **4**, eaau3402 (2018).
- [35] L. Petit, D. Paudyal, Y. Mudryk, K. A. Gschneidner, V. K. Pecharsky, M. Lüders, Z. Szotek, R. Banerjee, and J. B. Staunton, Complex magnetism of lanthanide intermetallics and the role of their valence electrons: Ab initio theory and experiment, *Phys. Rev. Lett.* **115**, 207201 (2015).
- [36] Y. J. Sato, H. Manako, Y. Homma, D. Li, R. Okazaki, and D. Aoki, New Gd-based magnetic compound GdPt_2B with a chiral crystal structure, *Physical Review Materials* **6**, 104412 (2022).
- [37] N. Yuan, A. Elghandour, W. Hergett, R. Ohlendorf, L. Gries, and R. Klingeler, 1/3 plateau and 3/5 discontinuity in the magnetization and the magnetic phase diagram of hexagonal GdInO_3 , *Physical Review B* **108**, 224403 (2023).
- [38] J. Sereni, I. Čurlík, M. Reiffers, and M. Giovannini, Evidence for magnetic dimers and skyrmion lattice formation in $\text{Eu}_2\text{Pd}_2\text{Sn}$, *Physical Review B* **108**, 014427 (2023).
- [39] A. Dutta, R. Jana, G. D. Mukherjee, and I. Das, Existence of short-range magnetic correlation and observation of large magnetocaloric effect in BiGdO_3 compound, *Journal of Alloys and Compounds* **846**, 156221 (2020).
- [40] J. A. Blanco, D. Gignoux, and D. Schmitt, Specific heat in some gadolinium compounds. II. Theoretical model, *Phys. Rev. B* **43**, 13145 (1991).
- [41] S. Pakhira, M. A. Tanatar, T. Heitmann, D. Vaknin, and D. C. Johnston, A-type antiferromagnetic order and magnetic phase diagram of the trigonal Eu spin- $\frac{7}{2}$ triangular-lattice compound EuSn_2As_2 , *Phys. Rev. B* **104**, 174427 (2021).
- [42] E. Sampathkumaran, I. Das, R. Rawat, and S. Majumdar, Magnetocaloric effect in Gd_2PdSi_3 , *Applied Physics Letters* **77**, 418 (2000).
- [43] E. V. Sampathkumaran and I. Das, Enhancement of heat capacity above the néel temperature in $\text{gd}_{1-x}\text{y}_x\text{ni}_2\text{si}_2$ alloys, and its implications, *Phys. Rev. B* **51**, 8178 (1995).
- [44] V. Chandragiri, K. K. Iyer, and E. Sampathkumaran, Magnetic behavior of $\text{Gd}_3\text{Ru}_4\text{Al}_{12}$, a layered compound with distorted kagomé net, *Journal of Physics: Condensed Matter* **28**, 286002 (2016).
- [45] R. Mallik, E. Sampathkumaran, M. Strecker, and G. Wortmann, Observation of a minimum in the temperature-dependent electrical resistance above the magnetic-ordering temperature in Gd_2PdSi_3 , *Europhysics Letters* **41**, 315 (1998).
- [46] R. Kumar, K. K. Iyer, P. L. Paulose, and E. V. Sampathkumaran, Magnetic and transport anoma-

- lies in $R_2\text{RhSi}_3$ ($r = \text{Gd, Tb, and Dy}$) resembling those of the exotic magnetic material Gd_2PdSi_3 , *Phys. Rev. B* **101**, 144440 (2020).
- [47] T. Samanta, I. Das, and S. Banerjee, Comparative studies of magnetocaloric effect and magnetotransport behavior in GdRu_2Si_2 compound, *Journal of Applied Physics* **104** (2008).
- [48] M. Hirschberger, T. Nakajima, S. Gao, L. Peng, A. Kikkawa, T. Kurumaji, M. Kriener, Y. Yamasaki, H. Sagayama, H. Nakao, *et al.*, Skyrmion phase and competing magnetic orders on a breathing kagomé lattice, *Nature communications* **10**, 5831 (2019).
- [49] N. D. Khanh, T. Nakajima, X. Yu, S. Gao, K. Shibata, M. Hirschberger, Y. Yamasaki, H. Sagayama, H. Nakao, L. Peng, *et al.*, Nanometric square skyrmion lattice in a centrosymmetric tetragonal magnet, *Nature Nanotechnology* **15**, 444 (2020).
- [50] L. J. Bannenberg, F. Weber, A. J. E. Lefering, T. Wolf, and C. Pappas, Magnetization and ac susceptibility study of the cubic chiral magnet $\text{Mn}_{1-x}\text{Fe}_x\text{Si}$, *Phys. Rev. B* **98**, 184430 (2018).
- [51] L. J. Bannenberg, A. J. E. Lefering, K. Kakurai, Y. Onose, Y. Endoh, Y. Tokura, and C. Pappas, Magnetic relaxation phenomena in the chiral magnet $\text{Fe}_{1-x}\text{Co}_x\text{Si}$: An ac susceptibility study, *Phys. Rev. B* **94**, 134433 (2016).
- [52] H. Wilhelm, M. Baenitz, M. Schmidt, U. K. Rößler, A. A. Leonov, and A. N. Bogdanov, Precursor Phenomena at the Magnetic Ordering of the cubic helimagnet FeGe , *Phys. Rev. Lett.* **107**, 127203 (2011).
- [53] A. Bauer and C. Pfleiderer, Magnetic phase diagram of MnSi inferred from magnetization and ac susceptibility, *Physical review B* **85**, 214418 (2012).
- [54] T. Kurumaji, T. Nakajima, M. Hirschberger, A. Kikkawa, Y. Yamasaki, H. Sagayama, H. Nakao, Y. Taguchi, T.-h. Arima, and Y. Tokura, Skyrmion lattice with a giant topological hall effect in a frustrated triangular-lattice magnet, *Science* **365**, 914 (2019).
- [55] V. Kumar, N. Kumar, M. Reehuis, J. Gayles, A. S. Sukhanov, A. Hoser, F. m. c. Damay, C. Shekhar, P. Adler, and C. Felser, Detection of antiskyrmions by topological Hall effect in Heusler compounds, *Phys. Rev. B* **101**, 014424 (2020).
- [56] P. V. P. Madduri, S. Sen, B. Giri, D. Chakrabartty, S. K. Manna, S. S. P. Parkin, and A. K. Nayak, ac susceptibility study of magnetic relaxation phenomena in the antiskyrmion-hosting tetragonal $\text{Mn} - \text{Pt(Pd)} - \text{Sn}$ system, *Phys. Rev. B* **102**, 174402 (2020).
- [57] N. Nagaosa, J. Sinova, S. Onoda, A. H. MacDonald, and N. P. Ong, Anomalous hall effect, *Reviews of modern physics* **82**, 1539 (2010).
- [58] Y. Tian, L. Ye, and X. Jin, Proper Scaling of the anomalous Halleffect, *Phys. Rev. Lett.* **103**, 087206 (2009).
- [59] S. Onoda, N. Sugimoto, and N. Nagaosa, Quantum transport theory of anomalous electric, thermoelectric, and thermal Hall effects in ferromagnets, *Phys. Rev. B* **77**, 165103 (2008).
- [60] T. Miyasato, N. Abe, T. Fujii, A. Asamitsu, S. Onoda, Y. Onose, N. Nagaosa, and Y. Tokura, Crossover behavior of the Anomalous Hall Effect and anomalous nernst effect in itinerant ferromagnets, *Phys. Rev. Lett.* **99**, 086602 (2007).
- [61] S. Onoda, N. Sugimoto, and N. Nagaosa, Intrinsic Versus Extrinsic Anomalous Hall Effect in Ferromagnets, *Phys. Rev. Lett.* **97**, 126602 (2006).
- [62] R. Ritz, M. Halder, C. Franz, A. Bauer, M. Wagner, R. Bamler, A. Rosch, and C. Pfleiderer, Giant generic topological hall resistivity of MnSi under pressure, *Phys. Rev. B* **87**, 134424 (2013).
- [63] J. Rowland, S. Banerjee, and M. Randeria, Skyrmions in chiral magnets with rashba and dresselhaus spin-orbit coupling, *Phys. Rev. B* **93**, 020404 (2016).
- [64] Y. Shiomi, S. Iguchi, and Y. Tokura, Emergence of topological Hall effect from fanlike spin structure as modified by Dzyaloshinsky-Moriya interaction in MnP , *Phys. Rev. B* **86**, 180404 (2012).
- [65] S. X. Huang and C. L. Chien, Extended skyrmion phase in epitaxial FeGe(111) thin films, *Phys. Rev. Lett.* **108**, 267201 (2012).
- [66] M. Onoda, G. Tatara, and N. Nagaosa, Anomalous Hall effect and skyrmion number in real and momentum spaces, *Journal of the Physical Society of Japan* **73**, 2624 (2004).
- [67] T. Kikuchi, T. Koretsune, R. Arita, and G. Tatara, Dzyaloshinskii-moriya interaction as a consequence of a doppler shift due to spin-orbit-induced intrinsic spin current, *Phys. Rev. Lett.* **116**, 247201 (2016).
- [68] A. A. Zyuzin, S. Wu, and A. A. Burkov, Weyl semimetal with broken time reversal and inversion symmetries, *Phys. Rev. B* **85**, 165110 (2012).